Motion of Quantum Vortices on Inhomogeneous Backgrounds

Peter Mason and Natalia G. Berloff
Department of Applied Mathematics and Theoretical Physics,
University of Cambridge, Wilberforce Road, Cambridge, CB3 0WA, United Kingdom
(Dated: February 1, 2008)

The motion of quantized vortices on two-dimensional inhomogeneous density backgrounds with boundaries is considered numerically and asymptotically. We show that a Hamiltonian group relation together with the method of images and an approximation for the density background is useful to understand vortex motion. We analyze the vortex motion on a variety of background configurations motivated by experiments on trapped Bose-Einstein condensates including linear and quadratic traps. We show that close to the center of the condensate cloud in the Thomas-Fermi regime the vortex is moving predominantly due to the image vortex that is effectively shifted because of the large density depletion of the condensate at the boundary. Close to the boundary the vortex moves mostly due to a large background density gradient across the vortex core. The vortex velocity is a nonlinear combination of these effects and of a global shape of the background density. We find the complete families of the traveling coherent structures in an infinitely long two-dimensional channel and derive an approximation of the velocity of a single vortex moving close to the center of the channel in the Thomas-Fermi regime.

PACS numbers: 03.65.Ca, 03.75.Lm, 05.45.-a, 67.40.Vs

I. INTRODUCTION

One of the fundamental questions in nonlinear sciences is the behavior of topological defects which owe their existence and perseverance to the topology of the order parameter describing a medium with a broken symmetry [1]. The motion of such defects on a spatially inhomogeneous backgrounds is studied in superconductivity, superfluidity and nonlinear optics. The motion of vortices in superconductors is influenced by localized inhomogeneities. External traps is a source of background density variations in Bose-Einstein condensates (BECs) and variations of the intensity in the beam cross-section create an inhomogeneous background in nonlinear optics experiments. The dynamics of quantum vortices and solitary waves in trapped Bose-Einstein condensation (BEC) has been a subject of intense interest since the first BEC realization in 1995. Numerous experiments have revealed the fascinating nature of these objects, in particular vortices [2, 3] and dark solitons [4–8]. Extensive work on the vortex dynamics in a trapped condensate has been the focus of much research (see for an overview [9–11]).

The problem of vortex motion on gradually varying backgrounds, such that the background field does not change considerably at the vortex core scale, can be treated using the method of matched asymptotic expansions [12, 13]. The small parameter of the expansion is associated with the background variation. In particular, it was established that the vortex is expected to move in the direction orthogonal to the gradient of the background density with a (slow) velocity proportional to the magnitude of the gradient of the logarithm of the background density. Unfortunately, there is no universal mobility relation as was emphasized in [1], so the detailed asymptotic expansion procedure has to be carried out for each particular system. Notably, this task has been achieved for the linear density background in a semi-infinite system by Anglin [14] again under the assumption that the vortex core size is much smaller than the distance of the density background variation and assuming that the vortex is far from the surface (boundary) of the condensate cloud.

A separate question concerns the effects of the boundaries on the vortex motion. In classical inviscid hydrodynamics the relevant kinematic boundary condition at a solid wall with normal vector $\mathbf{n}$ is

$$\rho\,\mathbf{u}\cdot\mathbf{n}=0, \tag{1}$$

where ρ is the local density of the fluid and $\mathbf{u}$ is the velocity of the fluid. This condition with non-zero values of the density of the classical fluid reduces (1) to a no-flow condition $\mathbf{u}\cdot\mathbf{n}=0$, which is often dealt with by introducing an image vortex of opposite circulation on the other side of the boundary and removing the boundary. It appears that for a condensate, with an order parameter which forces ρ to vanish on the boundary, the condition of no mass flow (1) is automatically satisfied and, therefore, the images are irrelevant to the dynamical description [14]. On the other hand, the method of images has been used in a number of papers that study two-dimensional vortex motion in condensates [15]. In [16] it has been shown that indeed a stronger condition $\mathbf{u}\cdot\mathbf{n}=0$ has to be satisfied on the solid (impermeable) boundary, so that the image vortices together with a good approximation of the background field is a useful tool in analyzing the vortex dynamics. In order to separate the effect of the surface from the effect of the density gradient, the dynamics of a vortex in a half space bounded by a solid wall on which the density of the condensate vanishes was an-

alyzed. This geometry represents the simplest problem of a vortex in a condensate interacting with a surface. Specifically, it was found that the depleted surface layer induces an effective shift in the position of the image in comparison with the case of a uniform flow, so that the velocity of the vortex can be approximated by

$$U \approx \frac{\hbar}{2m(y_0 - \sqrt{2}\xi)}, \tag{2}$$

where y_0 is the distance from the vortex core to the wall, ξ is the healing length of the condensate and m is the mass of the boson. Note that $\sqrt{2}$ corresponds to the area of the density depleted by the boundary layer, scaled by the density of the homogeneous state away from the vortex: $\int_0^\infty 1 - \tanh(y/\sqrt{2})^2\, dy = \sqrt{2}$.

The aim of this paper is to consider essentially *inhomogeneous* two-dimensional condensates in the presence of a boundary. We emphasize that although the problem of finding the leading order (logarithmic) term of the vortex velocity in trapped condensates has been successfully solved in [9, 17] and more recently in [18], we are interested in the correction to this expression. This correction will provide a dominant contribution to the vortex velocity when it is positioned close to the center of the condensate cloud and close to the condensate boundary. We shall also show that the vortex velocity is *not* equal to the sum of the local fluid velocity and a correction due to the background density gradient in the vortex core region. We shall restrict ourselves to the Thomas-Fermi (TF) regime in which the boundary of the condensate is better defined.

An analysis of the motion of vortices in trapped condensates will be presented in order to elucidate the relative importance that the density gradient and the image vortex has on the motion. Three separate cases will be considered, that gradually increase the complexity of the inhomogeneity. Firstly, we consider the vortex motion in a linear potential, which is a good estimate of the form of a condensate near the TF surface of the quadratic trapping potential [19]. A linear trap has also been used experimentally [20]. To consider a linear trap has the advantage that while the dynamics take place on an inhomogeneous density background there is a constant density gradient. Secondly, we consider a one-dimensional semi-infinite harmonic trap, so that the condensates' ground state (lowest energy state for a given number of particles) is strongly inhomogeneous near the boundary and approaches a constant away from the boundary. Finally, we find the complete families of traveling coherent structures in elongated traps in 2D. These waves have been the subject of a number of experimental [6–8, 21] and theoretical works in recent years, particularly in a three-dimensional axisymmetric cigar shaped trap [22–24] and in 2D channels [25, 26]. Collisions of solitary waves in 3D channels have also been elucidated [27].

The paper is organized as follows. In Sec. II we formulate the models that will be considered in this paper together with the numerical and asymptotic techniques used. In Sec. III we study the motion of a single vortex parallel to the TF boundary and calculate its velocity as a function of distance from the boundary. We analyze the vortex motion in a semi-infinite quadratic trap in Sec. IV and finally in Sec. V the family of coherent structures including vortices moving with a constant velocity in a channel for various strengths of interaction potential are found together with an asymptotic approximation to their motion. Section VI contains a summary of the main findings.

II. FORMULATION AND METHODOLOGY

The time-dependent Gross-Pitaevskii (GP) equation gives an accurate description of the dynamics of the Bose-Einstein condensate. For a two-dimensional condensate in an external potential, $V_{tr}(x, y)$, the GP equation is given in terms of the macroscopic wavefunction $\psi = \psi(x, y, t)$ by

$$\mathrm{i}\hbar\frac{\partial\psi}{\partial t} = -\frac{\hbar^2}{2m}\nabla^2\psi - (E_v - V_{tr}(x, y) - U_0|\psi|^2)\psi, \tag{3}$$

where E_v is the chemical potential of the system and U_0 is the two dimensional coupling constant in the disk-shaped geometry of the cloud [28]. The background inhomogeneity of the condensate cloud is provided by the external potential trap $V_{tr}(x, y)$, typically of the form

$$V_{tr}(x, y) = \frac{1}{2}m(\omega_x^2 x^2 + \omega_y^2 y^2), \tag{4}$$

where ω_x and ω_y are the frequencies associated with the respective coordinates of the trap.

We consider three different trap configurations that allow us to elucidate the effects of inhomogeneous backgrounds. Firstly, we consider a linear trapping potential. Near the surface of a condensate in a harmonic trap (4) Eq. (3) can be replaced by its linear approximation [19] via

$$V_{tr}(y) = E_v - \frac{1}{2}\gamma y, \tag{5}$$

where $\gamma = m\omega^2 R$ with Thomas-Fermi (TF) radius R and where we let $\omega \equiv \omega_x = \omega_y$. Thus, this expression for the potential, taken with the full dimensional GP equation (3) and scaled according to

$$\psi \to \sqrt{\frac{\epsilon\gamma}{U_0}}\psi, \qquad t \to \frac{\hbar}{2\epsilon\gamma}t, \qquad \boldsymbol{x} \to \epsilon\boldsymbol{x}, \tag{6}$$

where

$$\epsilon = \left(\frac{\hbar^2}{2m\gamma}\right)^{1/3}, \tag{7}$$

produces the non-dimensional GP equation for a condensate in a linear potential trap

$$2i\frac{\partial\psi}{\partial t} = -\nabla^2\psi - (\mu - V(y) - g|\psi|^2)\psi, \tag{8}$$

where $\mu = 1$ and $g = 1$ and

$$V(y) = 1 - \frac{1}{2}y. \tag{9}$$

Secondly, we consider a semi-infinite condensate in a one-dimensional quadratic external potential trap, that is switched off at large distances. Therefore, taking the GP equation (3) together with the one-dimensional quadratic potential,

$$V_{tr}(y) = \begin{cases} m\omega^2 y^2/2 & y \le 0 \\ 0 & y > 0 \end{cases} \tag{10}$$

and applying the scaling

$$\psi \to \sqrt{\frac{E_v}{U_0}}\psi, \qquad t \to \frac{\hbar}{2E_v}t, \qquad \boldsymbol{x} \to \frac{\hbar}{\sqrt{2mE_v}}\boldsymbol{x} \tag{11}$$

gives (after the transformation $y \to y - q$) the non-dimensional GP equation (8) with semi-infinite quadratic potential

$$V(y) = \begin{cases} \frac{1}{q^2}(y-q)^2 & y \le q \\ 0 & y > q \end{cases} \tag{12}$$

where the dimensionless parameter $q = 2E_v/\omega\hbar$ splits the background density into an inhomogeneous part (for $y \le q$) and a homogeneous part (for $y > q$) and $\mu = g = 1$ in Eq. (8).

In the final case to be investigated, namely the dynamics of vortices and other traveling coherent structures in an infinitely long channel with a one-dimensional quadratic potential $V_{tr}(y) = m\omega^2 y^2/2$, we use the scaling

$$\psi \to \frac{n^{1/2}}{a_\perp}\psi, \quad t \to \frac{1}{\omega}t, \quad \boldsymbol{x} \to a_\perp \boldsymbol{x}, \tag{13}$$

where $a_\perp = (\hbar/m\omega)^{1/2}$ is the transverse oscillator length and n is the number density of the ground state per unit length in the longitudinal direction. This non-dimensionalization gives Eq. (8), where $g = 2U_0 n/\hbar\omega a_\perp^2$. The chemical potential $\mu = 2E_v/\hbar\omega$ is fixed by the normalization condition

$$\int_{-\infty}^{\infty} |\psi_0|^2 dy = 1, \tag{14}$$

where $\psi_0(y)$ is the ground state of the condensate. The trapping potential in Eq. (8) becomes

$$V(y) = y^2. \tag{15}$$

We are interested in finding traveling coherent structures as solutions of (8) that preserve their form as they move subject to a potential $V(y)$ with a fixed velocity U. A moving vortex or a vortex pair are two particular examples of structures we seek to find. For each value of U, therefore, $\psi(x, y, t) = \psi(\eta, y)$, where $\eta = x - Ut$. Thus $\partial_t \to -U\partial_x$ in Eq. (8) gives

$$2iU\frac{\partial\psi}{\partial x} = \nabla^2\psi + (\mu - V(y) - g|\psi|^2)\psi \tag{16}$$

where without loss of generality we assign $x = \eta$, and all systems are solved subject to boundary conditions

$$\psi(x, y, t) \to \psi_0(y) \quad \text{as} \quad x \to \pm\infty. \tag{17}$$

We shall be interested in the form of the solutions (in particular the distance of the vortex from the condensate surface), its impulse p, velocity U, and energy E. For semi-infinite (in the $y-$direction) condensates (with a linear (9) or a semi-quadratic (12) traps) the impulse is defined [29] to be

$$p = \tfrac{1}{2i}\int \left[(\psi^* - \psi_0^*)\tfrac{\partial\psi}{\partial x} - (\psi - \psi_0)\tfrac{\partial\psi}{\partial x}^*\right] dxdy. \tag{18}$$

For the case of an infinitely long 2D channel, the phases of the solution may differ at $x \to +\infty$ and at $x \to -\infty$, so the impulse per unit length in the $z-$ direction is defined as in [22–24] via

$$\begin{aligned} p \;=\; & \int (|\psi|^2 - |\psi_0|^2)\frac{\partial\phi}{\partial x}\,dxdy = \\ & \frac{1}{2\mathrm{i}}\int \left[\psi^*\frac{\partial\psi}{\partial x} - \psi\frac{\partial\psi}{\partial x}^*\right] dxdy \\ - \; & \int |\psi_0|^2[\phi(x=\infty, y) - \phi(x=-\infty, y)]\,dy, \end{aligned} \tag{19}$$

where ϕ is the phase of $\psi = |\psi|\exp[i\phi]$.

The associated energy functional per unit length in the $z-$ direction is

$$E_f = \tfrac{1}{2}\int \left[|\boldsymbol{\nabla}\psi|^2 + (V(y) - \mu)|\psi|^2 + \tfrac{g}{2}|\psi|^4\right] dxdy\,. \tag{20}$$

The excitation energy suitably modified to accommodate the ground state ψ_0 is given by

$$E = E_f - E_{f_0}\,, \tag{21}$$

where E_{f_0} is the energy Eq. (20) evaluated at the ground state $\psi = \psi_0$ in the absence of the disturbance.

The solutions are found numerically by a Newton-Raphson iteration technique. The infinite domain is

mapped by the transformations $\widehat{x} = \tan^{-1}(Dx)$ and $\widehat{y} = \tan^{-1}(Dy)$ to a finite grid $(-\frac{\pi}{2}, \frac{\pi}{2}) \times (-\frac{\pi}{2}, \frac{\pi}{2})$. D is a constant chosen to lie in the range $D \sim 0.4 - 0.8$. The resulting equations are expressed in second-order finite-difference form. Taking 201^2 grid points in the finite domain, the resulting non-linear equations are solved by a Newton-Raphson iteration procedure using a banded matrix linear solver based on the bi-conjugate gradient stabilized iterative method. The accuracy of the obtained solutions is verified by evaluating various integral identities. The vortex position is detected by finding the zeros of the real and imaginary parts of the wavefunction. Note, that as the vortex moves close to the condensate boundary it becomes impossible to detect numerically whether we have a vortex solution or a rarefaction wave first introduced by Jones and Roberts [29] in the context of a uniform condensate. Rarefaction waves can be viewed as two-dimensional density depletions or finite amplitude sound waves with a dipole velocity field. The circulation around any contour for these solutions is zero. We shall, therefore, indicate the critical velocity at which we do not see numerically the difference between the two waves.

We compare the results of the numerics with the asymptotic expressions for the velocity of the solutions. To obtain this approximation we extend the method developed for a semi-infinite uniform condensate in a presence of a solid wall [16]. The idea is to employ the Hamiltonian group relation

$$U = \frac{\partial E}{\partial p}, \tag{22}$$

which is satisfied by classical vortex pairs and vortex rings as well as the quantum counterparts in BECs moving on homogeneous backgrounds [29]. The same result can be shown to be valid for traveling coherent structures satisfying (16). The variation $\psi \to \psi + \delta\psi$ in (18) and (19) results in the same form for δp, namely

$$\delta p = \mathrm{i} \int \delta\psi \frac{\partial \psi^*}{\partial x} - \delta\psi^* \frac{\partial \psi}{\partial x}\, dxdy \tag{23}$$

and in (21) produces

$$\begin{aligned} \delta E = & \tfrac{1}{2} \int \delta\psi^* \left[-\nabla^2\psi + \psi \left(V(y) - \mu + g|\psi|^2 \right) \right] + \\ & \delta\psi \left[-\nabla^2\psi^* + \psi^* \left(V(y) - \mu + g|\psi|^2 \right) \right] dxdy\,, \end{aligned} \tag{24}$$

provided $\delta\psi \to 0$ as $y \to \infty$. It follows that $\delta E = U\delta p$ and thus the Hamiltonian group relation of the energy and impulse taken along the sequence of solitary-waves holds for a general μ, g and $V(y)$. An alternative and useful form of the energy functional can be obtained from the substitution $x \to cx$, for a constant c in Eqs. (21) and (18). Then using the variational relationship

$$\frac{\partial}{\partial c} \delta \Big(E - Up \Big) \Big|_{c=1} = 0 \tag{25}$$

gives

$$E = \int \left| \frac{\partial \psi}{\partial x} \right|^2 dxdy\,. \tag{26}$$

To obtain an approximation to the velocity U as a function of y_0, Eq. (22) is rewritten as

$$U = \frac{\partial E}{\partial p} = \frac{\partial E / \partial y_0}{\partial p / \partial y_0} \tag{27}$$

with the form of the impulse and energy given by Eqs. (18), (19) and (26). Eqs. (22) and (26) are used to verify the numerical procedure. A trial wavefunction for a single vortex of a positive unit of circulation moving a distance y_0 from a condensate surface with a constant velocity is given by

$$\psi = \psi_{TF} \psi_{v_+} \psi_{v_-}, \tag{28}$$

where ψ_{TF} is the ground state, ψ_0, in the TF approximation, and the wavefunction of a vortex, ψ_{v_+}, and its image ψ_{v_-}, are given respectively by (see for example [16, 30])

$$\psi_{v_\pm} = \frac{x \pm \mathrm{i}(y \mp y_0)}{\sqrt{x^2 + (y \mp y_0)^2 + 2\xi_0^2}}. \tag{29}$$

Here the healing (coherent) length ξ_0 determines the size of the vortex core. For this form of the trial function, the expressions for the energy (26) and impulse (18,19) can be integrated exactly and expanded in large values of y_0. Note, that the approximation (28) is accurate only if the vortex is sufficiently far from the condensate surface. Typically a first order expansion of U in y_0 will guarantee a good approximation.

To separate a local effect of the density variation on the vortex motion we also compare the velocities obtained from the trial function (28) with those obtained from

$$\psi = \psi_{TF} \psi_{v_+}, \tag{30}$$

where the image vortex is absent.

III. LINEAR POTENTIAL

The first system considered in this paper is that of the dynamics of the Bose-Einstein condensate placed in a linear potential trap described by Eqs. (16) and (9).

This system has already been considered by Anglin [14] who used a boundary-layer approach to evaluate the vortex motion using the hydrodynamic (outer) solution and

the perturbative (inner) solution. It has been revisited by Al Khawaja [30] who used the form of Anglin's inner solution with a fitting parameter that was evaluated via numerical and variational calculations. The numerics involved forward integration in time of Eq. (16) with (9) on a truncated domain. The conclusion of [30] that the result obtained is superior to that of Anglin [14] has not been confirmed by our more rigorous numerical analysis. Conversely the result of Anglin [14] is accurate for even short distances from the condensate boundary; see Fig. 3 below.

Traveling coherent structures for positive velocity U are found by the numerical scheme introduced previously with the initial state given by Eqs. (28, 29). Figure 1 shows the energy, E, calculated from Eq. (21) (or Eq. (26)) as a function of the impulse, p, given by Eq. (18). For small U and large E and p, the solutions resemble a single vortex propagating at constant speed U, parallel to the x axis. As the velocity is increased the vortex drifts towards the boundary of the condensate until the velocity reaches $U \approx 0.73$ at which point we can no longer distinguish between the vortex solution and the rarefaction wave.

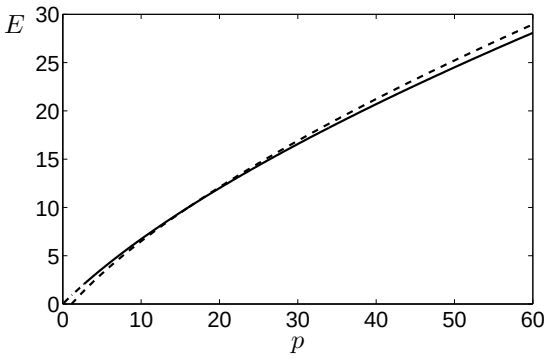

FIG. 1: The energy, E, as a function of impulse, p, of the traveling coherent structures of Eq. (16) with linear trapping potential (9). The solid line corresponds to a single vortex solution. The energy-impulse of rarefaction pulses are depicted by the dot-dashed line. Also shown (dotted line) is the energy vs impulse given by Eq. (31). Energy is measured in units of $\hbar^2\epsilon\gamma/mU_0$ and impulse in units of $\hbar\epsilon^2\gamma/U_0$.

We obtain the corresponding analytical approximations of the energy E, impulse p and velocity U as functions of the vortex distance y_0, from the condensate boundary (defined here as the boundary given by the TF profile) by following the procedure described in the previous section. We consider the trial function (28) with (29) and $\xi_0 = 1/|\psi_{TF}|$, where the TF ground state is $\psi_{TF} = \sqrt{y/2}$, as an approximation for a vortex solution assuming that y_0 is sufficiently large. Figure 2 shows that indeed Eqs. (28, 29), provide a good approximation to the exact numerical solution. For this choice of the trial function, the impulse (18) and energy (21) are exactly integrable in x and y and to the leading order in large y_0 become

$$E = \frac{\pi y_0}{4}\left(\frac{1}{2} + 3\ln(y_0)\right), \tag{31}$$

$$p = \frac{\pi y_0^2}{2}. \tag{32}$$

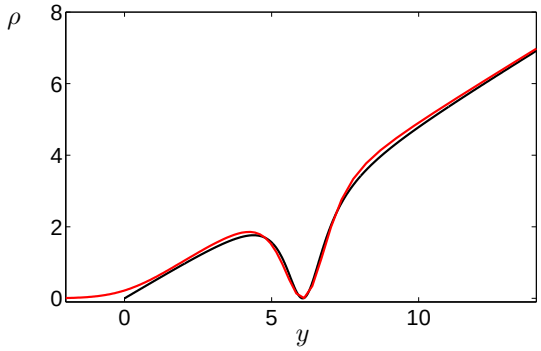

FIG. 2: (Color online) The density ($\rho = |\psi|^2$) for the trial function given by Eqs. (28)-(29) for a vortex solution of the Eq. (16) with the linear trapping potential (9) (black line) and the numerically exact solution (gray (red) line). The density is measured in $\epsilon\gamma/U_0$ and distance in ϵ.

The velocity is than evaluated according to Eq. (27) as

$$U_L = \frac{1}{2y_0}\left(\frac{7}{4} + \frac{3}{2}\ln(y_0)\right). \tag{33}$$

The above result can be compared to the result derived by Anglin [14]

$$U = \frac{1}{2y_0}\left(1.267 + \frac{3}{2}\ln(y_0)\right). \tag{34}$$

Both results are valid only for large y_0, i.e. far from the boundary. We show the exact numerical result for the velocity as a function of y_0 together with asymptotic results (33) and (34) in Fig. 3.

Note that compared to the precise numerics, the accuracy of the asymptotic approach taken here using the Hamiltonian group relation (22) provides as strong an approximation to the velocity profile as does the boundary layer approach taken by Anglin in [14]. In fact the leading order term in both expressions (33) and (34) has the same multiplying factor. However, the analysis undertaken here has explicitly included an image vortex as a mean of satisfying the no-flow condition. Hence it can be deduced that a vortex moves because of the combined effect of the density gradient and the 'shifted' image. While indeed the method of images is limited to cases of simple

geometry, it is an extremely useful tool to use when applicable and produces a result as accurate as a full matched asymptotic approach but with the additional benefit of simplicity.

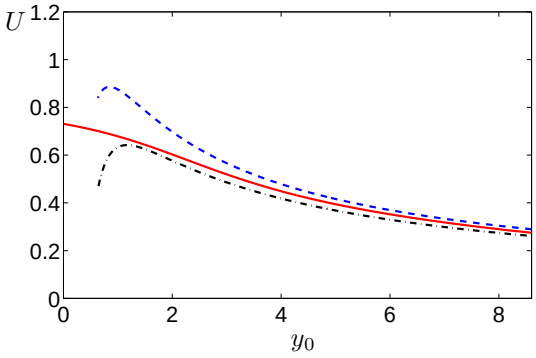

FIG. 3: (Color online) Graphs of the velocity of the vortex U vs. the vortex position y_0 calculated by a numerical integration of Eq. (16) subject to the boundary conditions (17) for the linear potential $V(y) = 1 - (y/2)$ (solid red curve) and the asymptotics given by (33) (dashed blue curve). The corresponding result of Anglin (dash-dot black curve) (34) is also given. Velocity is measured in units of $2\epsilon^2\gamma/\hbar$ and distance in units of ϵ.

In order to separate the effects of the local density variation from the boundary effects we calculate the motion of a vortex without the implied image. We take the trial function (30) and again use the Hamiltonian relation (22) to determine the vortex velocity. The wavefunction does not decay fast enough for the convergence on the half-plane in y, so we consider a finite integral over $y \in [0, \ell y_0]$, where $\ell \gg 1$ and asymptotically get the following expressions for the energy (21) and magnitude of the impulse (18)

$$E_1 = \frac{\pi y_0}{4}\left(\ell + 3\ln(y_0)\right), \tag{35}$$

$$p_1 = \frac{\pi \ell^2 y_0^2}{4}. \tag{36}$$

We also re-evaluate Eqs. (31)-(32) for the same finite domain in y to get

$$E = \frac{\pi y_0}{4}\left(\frac{1}{2} - \frac{2}{\ell} + 3\ln(y_0)\right), \tag{37}$$

$$p = \frac{\pi y_0^2}{2}. \tag{38}$$

By inspection we conclude that the logarithmic term in the energies comes from the local density variation, whereas the effect of the image vortex is represented by the term linear in y_0. It is also important to emphasize the nonlocal effects represented by the second term of Eq. (37), which leads to the correction to the velocity due to the finite integration domain

$$U = U_L - \frac{1}{2y_0\ell}. \tag{39}$$

Thus, the velocity of the vortex is not the sum of the local fluid velocity and a correction that describes the background density gradient in the vortex core region. Instead, (i) the total shape of the condensate has an influence on the vortex motion not just the background density in the vortex core and (ii) the effective position of the image is greatly modified by the shape of the condensate. The effects of the applied velocity (due to the image) and the contribution to the velocity (due to the background density gradient) do not combine linearly.

IV. SEMI-INFINITE QUADRATIC POTENTIAL

In this section we shall analyze vortex and other traveling coherent structures of Eq. (16) for the external trapping potential given by Eq. (12) and subject to the boundary conditions (17). The density profile is quadratic for $0 \le y \le q$ and constant for $y > q$. We are interested in how the vortex velocity changes as the vortex moves further away from the condensate surface. This is an intermediate case between the motion on a linear background density (considered in the previous section) and the case of a vortex moving in an untrapped condensate with a solid boundary considered in [16]. A good choice of q would be one that allows an appropriate range for the varying density background ($0 \le y \le q$) whilst at the same time reflects the ability of the numerics to resolve accurately around the vortex in the uniform density background range. The choice used here is $q = \sqrt{50}$.

Firstly, traveling coherent structures moving with velocity U are sought. As before, the same numerical scheme introduced in Sec. II can be utilized to find the energy and impulse of the solutions. The Ep dispersion curve is given in Fig. 4. For small velocity, the solution is a single vortex far away from the boundary of the condensate. As the velocity increases the vortex drifts towards the boundary, and for $U > 0.5$ ($E \approx 1.20$, $p \approx 2.18$) becomes indistinguishable from rarefaction waves.

The velocity profile can be found by employing the Hamiltonian group relation Eq. (22) with the form of the wavefunction given by Eqs. (28) and (29) where the ground state is

$$\psi_0(y) = \begin{cases} \sqrt{1 - \frac{1}{q^2}(y-q)^2} & 0 \le y \le q \\ 1 & y > q \\ 0 & \text{otherwise.} \end{cases} \tag{40}$$

Integration of the impulse and energy results in an

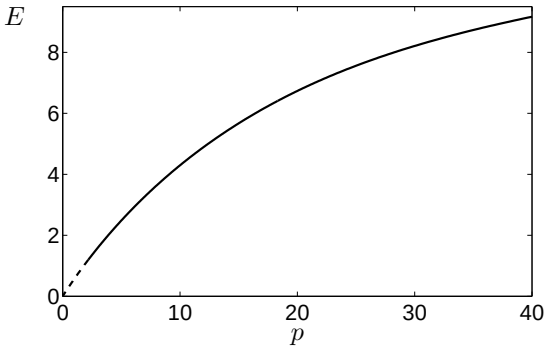

FIG. 4: The energy-impulse curve of the solitary-wave solutions of Eq. (16) with semi-infinite quadratic trapping potential Eq. (12). The solid line corresponds to a single vortex solution. The part of the Ep curve for $U > 0.5$ is depicted by the dashed line. Energy is measured in units of $\hbar^2 E_v/mU_0$ and impulse in units of $(\hbar^4 E_v/2mU_0^2)^{1/2}$ both per unit length in the $z-$direction.

second-order approximation of U in y_0^{-1}

$$U = \frac{1}{2y_0} + \frac{5\sqrt{2}}{3y_0^2} \tag{41}$$

valid for large y_0.

Alternatively, exploiting the similarity between the density profiles of this condensate and the one considered in [16] for a vortex next to a wall allows a more accurate estimate of the velocity profile. Following the analysis of [16], the velocity can be found by using the area of the displaced density

$$\int_0^\infty 1 - (1 - V(y))dy = \frac{5}{3}\sqrt{2}, \tag{42}$$

to recover

$$U = \frac{1}{2\left(y_0 - \frac{5}{3}\sqrt{2}\right)} \tag{43}$$

which has the same first two terms of the Taylor expansion as Eq. (41).

Figure 5 gives the plot of the vortex velocity U as a function of the distance of the vortex from the boundary y_0 for the numerically determined values, the approximation given by (43) and the exact Hamiltonian established from Eq. (22). The effects of the density gradient and the boundary can be readily seen. Far from the boundary, i.e. for large y_0 where $y > q$, Eq. (43) gives an accurate approximation to the velocity. In this region the density gradient is zero and thus the motion can be viewed as being due to a 'shifted' image vortex, with the shift caused by the large depletion in density around the boundary.

The exact Hamiltonian group relation (22) with (28) still gives a good approximation of the vortex motion in $0 \le y \le q$. In this region, the density gradient becomes more prevalent, and the exact Hamiltonian is found to be in good agreement with the numerics as Fig. 5 illustrates.

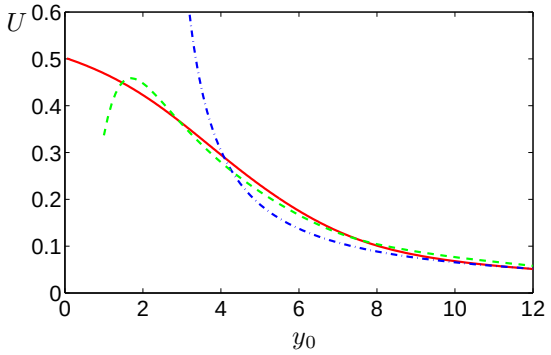

FIG. 5: (Color online) Graphs of the velocity of the vortex U vs. the vortex position y_0 calculated by a numerical integration of Eq. (16) subject to the boundary conditions (17) for the semi-infinite quadratic potential $V(y)$ given in Eq. (12) (solid red curve). Also shown is the velocity found by the Hamiltonian group relation (22) (dashed green curve) and the asymptotic expression (43) (dash-dot blue curve). Velocity is measured in units of $(2E_v/m)^{1/2}$ and distance in units of $\hbar/(2mE_v)^{1/2}$.

V. VORTICES IN A CHANNEL

In this section, we consider vortex dynamics in an infinitely long channel, a two-dimensional version of a three-dimensional cigar trap considered experimentally by [7, 8]. The dynamics of the three-dimensional cigar trap have also been investigated theoretically by [22, 23], who discovered a rich variety of traveling coherent structures, namely vortex rings and gray and black solitons. The dynamics of solitonic structures in trapped BEC's have also been widely studied (see for example [31–34]).

We consider the GP equation (16) with the potential given in (15) that describes the dynamics of traveling coherent structures in an infinitely long channel. In contrast with the previous sections $y = 0$ is identified with the center of the condensate rather than with its TF boundary. As before, the ground state ψ_0 can be estimated from the TF approximation (valid for large g)

$$\psi_{TF} = \left(\frac{\mu - y^2}{g}\right)^{1/2}, \tag{44}$$

for $\mu > y^2$ and zero otherwise. The width of the condensate is then $2\sqrt{\mu}$ and the center of the trap is along $y = 0$. It can be shown from (14) and (44) that $\mu^3 \sim 9g^2/16$.

By fixing the interaction strength, g, the corresponding chemical potential μ and ground state ψ_0 can be found exactly from a simple numerical iteration technique subject to the initial approximation (44) and to the normalization condition (14). A plot of the ground states for a range of values of g is given in Fig. 6.

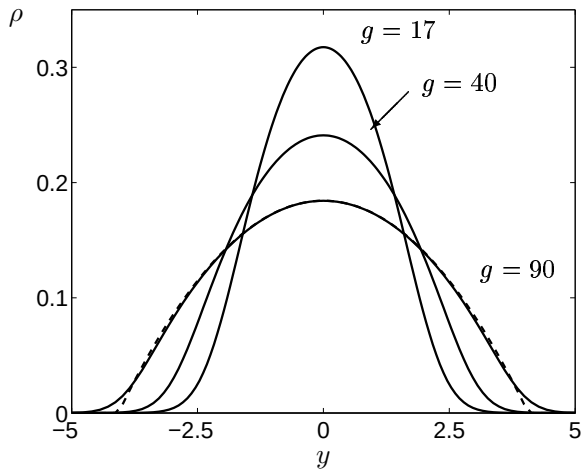

FIG. 6: The ground state density, $\rho = \psi_0^2$, for $g = 17$, $g = 40$ and $g = 90$ (solid lines) plotted against y. The Thomas-Fermi profile (44) for $g = 90$ is also given (dotted line). Density is measured in units of $n/a_\perp^2$, distance in units of $a_\perp$.

Traveling coherent structures were found numerically for various values of g. The solutions found are quite analogous to their three–dimensional (3D) counterparts found by Komineas and Papanicolaou [22–24]. We briefly discuss these solutions emphasizing the differences between our 2D solutions and the axisymmetric 3D solutions.

We also would like to clarify the difference between dark (gray, black) solitons and rarefaction pulses used in the context of the 2D and 3D channels. Both types of solutions represent a density depletion that propagates with a constant velocity, so their density profiles are quite similar. Nevertheless, they have quite a different phase structure when viewed along the axis of the propagation. The dark soliton is a soliton solution of the GP equation (16) in one dimension with $\mu = 1, g = 1, V(y) = 0, \nabla^2 = \partial_x^2$ and is found [35] explicitly as

$$\psi_d(x) = \mathrm{i}\frac{U}{c} + \sqrt{1 - \frac{U^2}{c^2}}\tanh\left[\frac{x}{\sqrt{2}}\sqrt{1 - \frac{U^2}{c^2}}\right], \qquad (45)$$

where the speed of sound $c = 1/\sqrt{2}$. Note, that if ψ_d is a solution of Eq. (16) then so is $i\psi_d$. If $U = 0$, the dark soliton (45) is called a black soliton, otherwise it is a gray soliton. The distinctive feature of the dark soliton is, therefore, a constant real or imaginary part. To the contrary, the rarefaction pulses (see, for the analytical approximations [36]) have both real and imaginary parts varying in space. One of the parts does not change sign, but its absolute value has a minimum at the center of the pulse.

A. Case Study 1: g=17

The first case to consider is for a low interaction strength, $g = 17$. This value of g gives the value of the chemical potential $\mu = 5.60$ found numerically. Initially, in order to clarify the dynamics of a single vortex and a pair of vortices, the energy-impulse curves will be plotted separately. The dispersion curve for a single vortex is shown in Fig. 7. The symmetry about $p = \pi$ and the 2π periodicity is as expected [22]. In the center of the condensate the solution corresponds to a single vortex with zero velocity (point A in Fig. 7). This branch is doubly degenerate as there is a solution with a vortex of opposite circulation with the same energy. As the velocity is increased the vortex with the positive circulation moves to negative y values (point B). It continues to do so as the velocity is increased further until at $U = 0.91$ we can no longer distinguish between a single vortex and a rarefaction pulse. The termination velocity (i.e. the velocity of U at which the traveling structures reach the edge of the condensate and terminate) is $c \sim 1.30$. This value of c can be approximated from $E \approx cp$ near the edge of the condensate. Exactly the same dynamics occurs for negative velocity, albeit with the single vortex now moving towards the upper channel boundary (positive values of y). To summarize the single vortex case, in the bulk of the condensate, for $|U| < 0.91$, (points A and B in Fig. 7) the solution is a single vortex.

The energy-impulse graph for a single vortex is qualitatively the same for all values of g. As g is increased the only discernible difference can be found in the decreasing range of values for which a rarefaction wave exists.

The dispersion curve for a pair of vortices is given in Fig. 8, where the termination speed is the same as for the single vortex case. The curve is qualitatively the same as the single vortex case, however in the bulk of the curve $|U| < 0.82$ the solutions correspond to a pair of vortices, one of positive circulation at $y = -y_0$ and one of negative circulation at $y = y_0$ (points A and B in Fig. 8 respectively). As energy increases the distance between vortices decreases until two vortices completely overlap, so that there is a single point where $\psi = 0$. This solution moves with $U = 0$ and is a black soliton. As the magnitude of the velocity is increased away from zero, the vortices drift away from the center of the trap until for $0.82 \leq |U|$ they lose their vorticity and become a pair of rarefaction waves (point C). The difference between the profiles of the rarefaction pulse and the dark soliton along the direction of propagation of the wave is shown in Fig. 9. A density contour plot is provided in Fig. 10

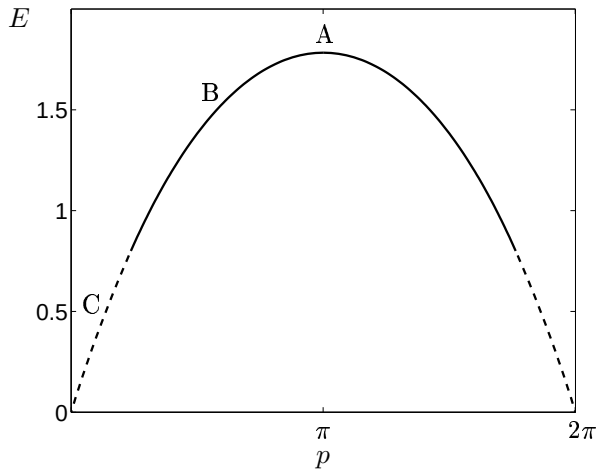

FIG. 7: The energy-impulse dispersion curve for $g = 17$ for a single vortex. The solid line corresponds to the single vortex solution, whereas the dotted line corresponds to a rarefaction wave for $0.91 \leq |U|$. Point A is at velocity $U = 0$, point B is at $U = 0.5$ and point C is at $U = 1$. These points are referred to in the text. Energy per unit length is measured in units of $\hbar n\omega$ and impulse in units of $\hbar n/a_\perp$.

for points B and C, and Fig. 11 gives the plots of the real and imaginary parts of the wavefunction taken across the channel. The positions of vortices are clearly seen in the top frame.

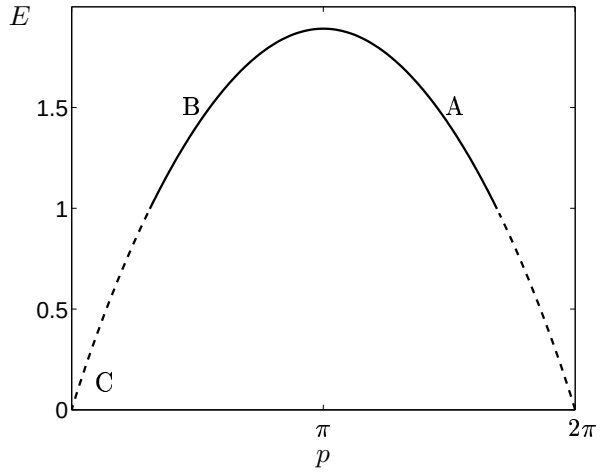

FIG. 8: The energy-impulse dispersion curve for $g = 17$ for a pair of vortices. The solid line corresponds to the two vortex solution, whereas the dotted line corresponds the rarefaction wave region. There is a black soliton at $U = 0$. Points A and B are at $U \mp 0.5$ respectively and point C is at velocity $U = 1$. The units of energy and impulse are as in Fig. 7.

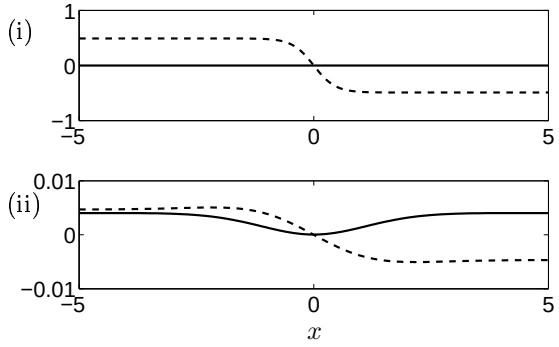

FIG. 9: The real (solid line) and imaginary (dotted line) components of the wavefunction for a black soliton (frame (i)) and a rarefaction pulse (frame (ii)) for a cross-section through the center of the wave along the direction of its propagation for $g = 17$ in the multi-vortex system are shown. The black soliton is for $U = 0$ and the rarefaction pulse is at $U = 0.9$. The distances are measured in $a_\perp$.

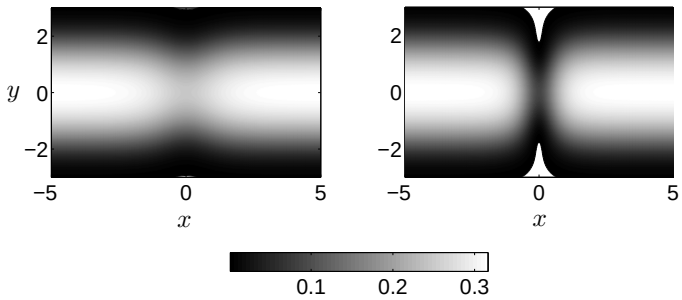

FIG. 10: Density ($\rho = |\psi^2|$) profiles for $g = 17$ for a pair of vortices in the xy plane. Right (left) panel corresponds to B (C) solutions shown in Fig. 8. Darker regions correspond to areas of low density whereas lighter regions correspond to areas of high density. Units are as in Fig. 6.

B. Case Study 2: g=40

As the interaction strength is increased, new features develop in the multi-vortex energy-impulse dispersion curve when $g \geq 23.3$. This value is the expected first critical coupling which has been numerically explored in axisymmetric 3D traps by [22]. For $g \geq 23.3$ a cusp develops in the dispersion curve at a critical coupling velocity. A regime can be classified, dependent on the parameter g, such that for $23.3 \leq g < 59.4$ there is a single cusp in the dispersion curve (ignoring symmetry about $p = \pi$).

The dispersion curve for a single vortex exhibits no such properties and remains qualitatively the same for all values of g, as is shown in Fig. 12. The new features of the multi-vortex solution are also shown in the dispersion curve in Fig. 12 for $g = 40$ (with corresponding chemical

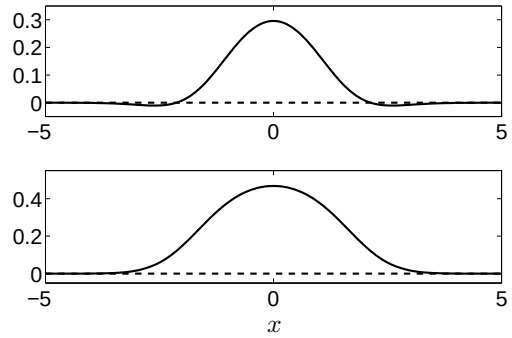

FIG. 11: The real (solid line) and imaginary (dashed line) parts of the wavefunction of the traveling wave solution for $g = 17$ taken across the channel at $x = 0$. Top (bottom) frame corresponds to point B (C) shown in Fig. 8. Units are as in Fig. 6.

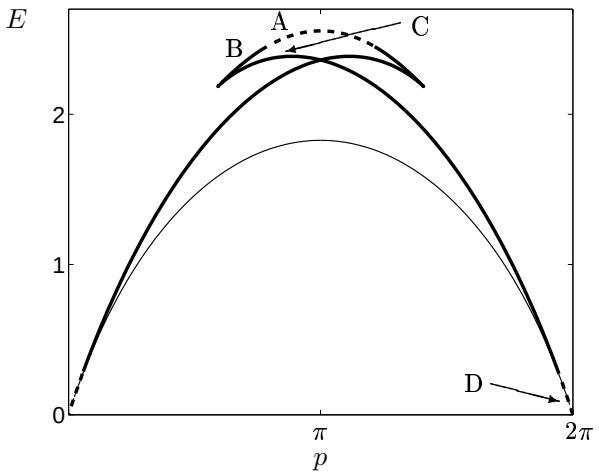

FIG. 12: The energy-impulse dispersion curve for $g = 40$. The thick solid line corresponds to the two vortex solution, whereas the dashed thick line corresponds the pair of rarefaction waves. There is a black soliton at $U = 0$. The thin solid line is the single vortex solution and the corresponding rarefaction wave. Points A, B, C and D are at velocities $U = 0.2$, $U = 0.4$, $U = 0$ and $U = -1.6$ respectively. The units of energy and impulse are as in Fig. 7.

potential value $\mu = 9.75$), where this particular value of g is chosen to illustrate the new features explicitly. At this particular value of g it can be seen that a cusp point develops at a critical coupling velocity of $U = 0.53$ (with a further cusp present at $U = -0.53$ by symmetry about $p = \pi$). The cusp introduces an extra branch into the family of traveling coherent structures. Two branches in the dispersion curve are here discussed. The remaining two can be found by symmetry about $p = \pi$.

At zero velocity and $p = \pi$ there is a black soliton. As the velocity is increased a pair of rarefaction pulses develop (point A in Fig. 12) which are maintained until $U = 0.3$ at which point a pair of vortices of opposite circulation form near the center of the condensate. Further increasing the velocity encourages the vortices to gradually drift apart (point B) until a velocity $U = 0.53$ at which the branch terminates. A cusp is then seen to develop. The velocity is now decreased and following the new branch, it is clear that the the two vortex solution present in the first branch is continuous through the cusp (see Fig. 14). Along this new branch the vortices continue to separate from one another. A configuration is eventually realized whereby the pair of vortices in the channel are stationary, $U = 0$ (point C). The velocity is then moved to negative values until $U = -1.47$ at which point the vortices lose their circulation and a pair of rarefaction waves develop (point D). The termination velocity for $g = 40$ is $c = 1.73$. A contour plot of the solutions that correspond to the four points A, B, C and D is shown in Fig. 13.

The velocity of pairs of vortices is shown in Fig. 14 as a function of the distance between one of the vortices and the center of the condensate. At the cusp, which occurs at $U = 0.53$, the smooth transition of the vortex motion from one branch to the other is evident.

Changing the value of g (provided it remains in the range $23.3 \leq g < 59.4$) will not alter the overall structure of the dynamics, but changes the value of the critical coupling velocity at which the cusp appears, with the critical coupling velocity increasing with increasing g. It will also alter the termination speed and furthermore the velocity of the onset of the rarefaction wave from a pair of vortices.

C. Case Study 3: g=90

If the interaction strength is further increased, another critical coupling is found to occur at $g = g_2 = 59.4$. A new regime can then be said to occur for interaction strengths $59.4 \leq g < 104.4$. This new regime is characterised by the formation of an additional cusp in the multi-vortex energy-impulse curve and thus the introduction of a new branch of solutions. Taking $g = 90$ as a clear example of this second regime, the extra features can again be best seen in the multi-vortex dispersion curve Fig. 15. The chemical potential is $\mu = 16.64$. Two cusps are present, one at $U = 0.66$ and the second at $U = -1.31$. The dynamics are now described along the three numerically computed branches that form the dispersion curve of which the sequence A, B, C, D in Fig. 15 is a component. As in previous examples, the other branches can be obtained by symmetry about $p = \pi$.

Starting with a black soliton at $U = 0$, a system of six vortices develops (point A in Fig. 15) so that there are

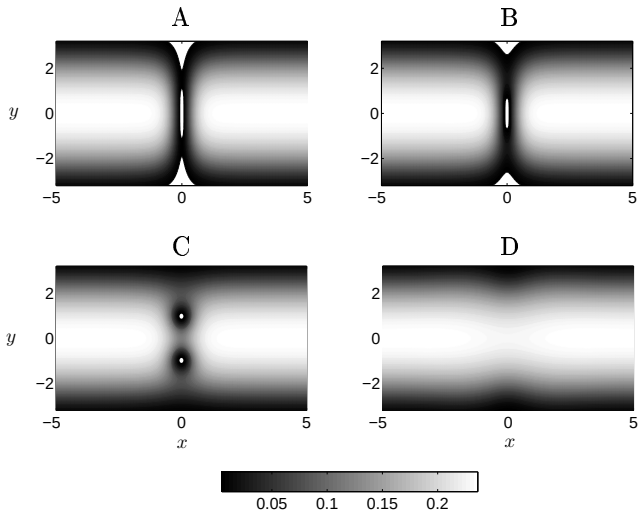

FIG. 13: Density profiles ($\rho = |\psi^2|$) for $g = 40$ for the multi-vortex solution in the xy plane. Darker regions correspond to areas of low density whereas lighter regions correspond to areas of high density. Points A, B, C and D are shown in Fig. 12. Units are as in Fig. 6.

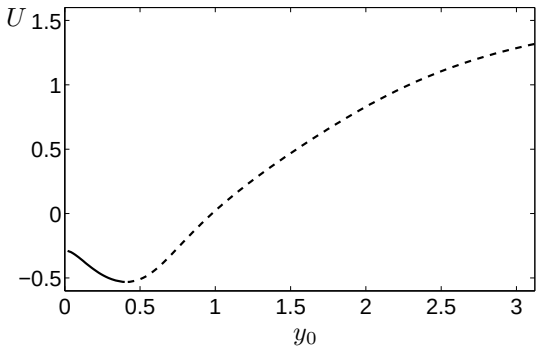

FIG. 14: Velocity, U, of the pair of vortices of opposite circulation as a function of y_0, which is the distance from the center of the condensate to one of the vortices for $g = 40$. The cusp, from Fig. 12 is at $U = -0.53$. Solutions on the upper branch are shown by the solid line and solutions on the lower branch are shown by the dotted line. Velocity is measured in units of $a_\perp\omega$ and distance in units of $a_\perp$.

six vortices of alternate circulations. As U is increased towards the first cusp, the two outermost vortices quickly move towards the edge of the condensate until $U = 0.48$ at which point these vortices disappear. In the meanwhile the inner 4 vortices, which can be divided up into two pairs of vortices, one pair on either side of the center of the condensate, creep slowly towards each other. However as the outer two vortices of the six are lost, the four remaining vortices now all begin to separate.

This process continues until the first cusp is reached at $U = 0.66$. The two inner most vortices continue to drift towards the center of the condensate and the outer two continue to drift towards the edge of the condensate, however at a much faster rate (point B). At $U = -1.28$, the outer two vortices reach the edge of the condensate and the system is reduced to a two vortex set-up. While still decreasing the velocity another cusp will be found at $U = -1.31$. If the new branch is tracked (and therefore the velocity increased) it is found that the two remaining vortices slowly drift apart towards the edge of the condensate (see points C and D). For large values of the velocity, $U \geq 1.85$, the two vortices colliding with their images form a pair of rarefaction waves which continue to propagate as the velocity is increased until the termination velocity is reached which for $g = 90$ is $c = 1.95$. A contour plot of the density for the four separate points A, B, C and D in the dispersion curve gives a clear indication of the dynamics.

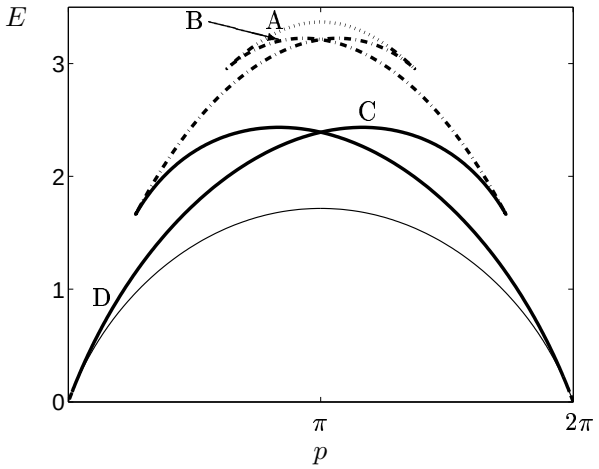

FIG. 15: The energy-impulse dispersion curve for $g = 90$. The thick solid line corresponds to the two vortex solution, whereas the dotted thick line corresponds the pair of rarefaction waves. The thick dot-dash line is the four vortex system and the thick short-dash line is the six vortex solution. There is a black soliton at $U = 0, p = \pi$. The thin solid line is the single vortex solution and the corresponding rarefaction wave. Points A, B, C and D are at velocities $U = 0.2$, $U = 0.1$, $U = 0$ and $U = 1.4$ respectively. The units of energy and impulse are as in Fig. 7.

D. Discussion

The interaction strength can be viewed as a measure of the density gradient of the condensate, with increasing interaction strength corresponding to a smaller density gradient particularly in the center of the condensate. There exists a series of critical coupling values of g and

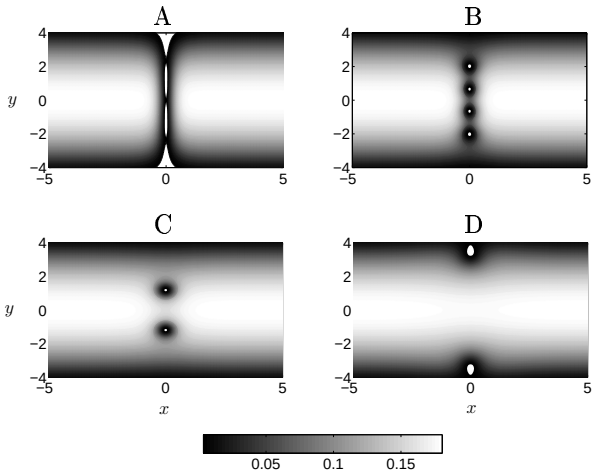

FIG. 16: Density profiles ($\rho = |\psi^2|$) for $g = 90$ for the multi-vortex solution in the xy plane. Darker regions correspond to areas of low density whereas lighter regions correspond to areas of high density. Points A, B, C and D are shown in Fig. 15. Units are as in Fig. 6.

the next two critical couplings occur at $g = g_3 \sim 104.4$ and $g = g_4 \sim 156.6$. As each new critical coupling is reached, an extra cusp will appear in the dispersion curve and therefore a new branch of solutions is formed.

The effect of raising g to even higher values would be two-fold. Firstly, as the density gradient decreases the effect that a 'shifted' image would have on the dynamics would increase. Near the center of the condensate the density gradient would become small and the effects, noticed in Sec. IV, come to prominence.

To obtain an approximation to the velocity of a vortex positioned close to the center of the condensate (small y_0) with large g we employ the method we described in Section II. We consider a trial function

$$\psi = \psi_{TF}\psi_v\psi_{v_1}\psi_{v_2}, \tag{46}$$

where ψ_{TF} is given by Eq. (44) and

$$\psi_v(x,y) = \frac{x + \mathrm{i}(y - y_0)}{\sqrt{x^2 + (y-y_0)^2 + 2/\mu}}. \tag{47}$$

Two images are given as

$$\psi_{v_1} = \psi_v^*(x, y - 2\sqrt{\mu} + 2y_0), \tag{48}$$
$$\psi_{v_2} = \psi_v^*(x, y + 2\sqrt{\mu} + 2y_0). \tag{49}$$

Ideally, one would need to introduce an infinite number of images to represent the no-flow condition at the boundaries [38], but our method only works in the TF regime for which the channel is wide and the effect of far away vortices is insignificant. For large g, this choice of the trial function accurately represents the density of the condensate in the entire domain, see Fig. 17. However it does not capture the phase difference at infinities, see Fig. 18, as for any y_0 the phase of (46) jumps by π. Note, that the infinite superposition of image vortices would give the correct phase difference different from π. Therefore, we can not expect the estimate of the impulse (19) to give an accurate result. But the expression for energy (26), that depends only on derivatives of ψ, gives an accurate estimate of the numerically obtained energy. We also note that $E(p)$ has a form of a parabola that we approximate on $[0, \pi]$ by

$$p = \pi\left(1 - \sqrt{1 - \tfrac{E}{E_{\max}}}\right), \tag{50}$$

where $E_{\max}$ is the maximum value of energy that occurs when the vortex is at the center of the channel, $y_0 = 0$. This, together with (27), yields the expression for the velocity as

$$U = \frac{2}{\pi}\sqrt{E_{\max}^2 - E_{\max}E}. \tag{51}$$

Figure 19 shows the comparison of our approximation (51) with numerically calculated values for $g = 100$ and $g = 500$.

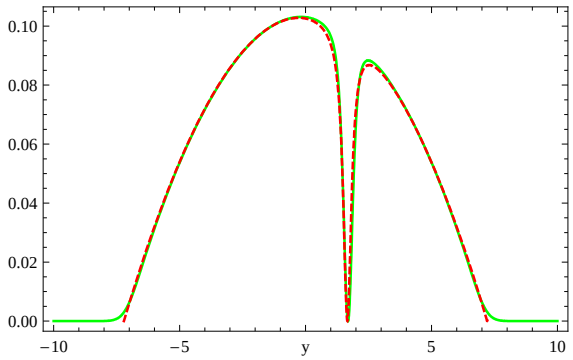

FIG. 17: (Color online) The density of the condensate for $g = 500$ at the cross-section $x = 0$ through the vortex center. The exact (numerical) density is shown in solid gray (green), the approximation (46) is shown by a dashed line. The vortex is positioned at $y_0 = 1.66$ away from the center of the channel and moves with the velocity $U = 0.2$. The distances are measured in $a_\perp$.

A second effect of raising g would be in the type and variety of the dynamics encountered. One could envision a dispersion curve with multiple cusps and multiple branches. The dynamics possible in such a system would be fairly impressive, but it seems certain that a few points can be made about the system. It has already been seen for relatively low values of g that the lower branch which terminates at the termination speed contains an ever decreasing range for which a pair of rarefaction waves exist. It is therefore natural to assume that as g is increased to

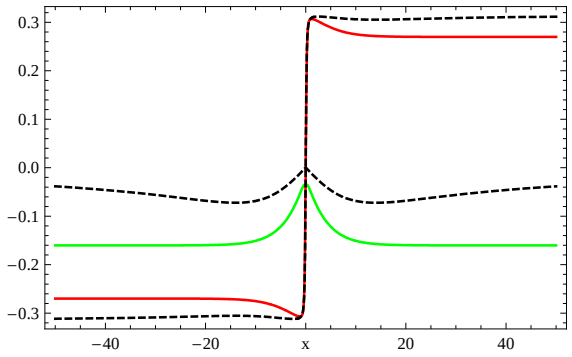

FIG. 18: (Color online) Real and imaginary parts of the condensate wavefunction for $g = 500$ at the cross-section $y = y_0$ through the vortex center. The vortex moves with the velocity $U = 0.2$. The exact (numerical) solutions are shown by solid lines (dark gray (red) – real part, light gray (green) – imaginary part), the approximations (46) are shown by dashed lines.

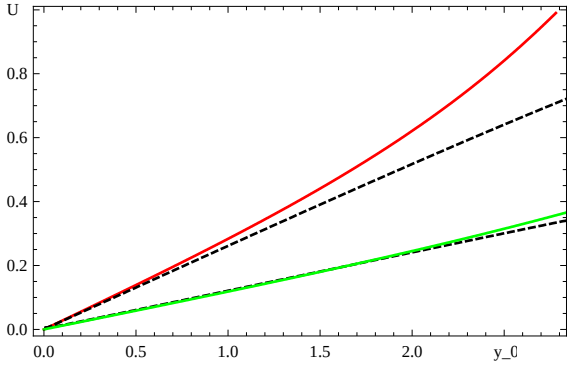

FIG. 19: (Color online) Velocity of a vortex as a function of the distance between the vortex and the center of the channel. Dark gray (red) solid curve corresponds to the numerical solution for $g = 100$, light gray (green) solid curve is for $g = 500$. Dashed lines show our approximation (51) where E is calculated from (26) using the trial function (46). The distances are measured in $a_\perp$. Note that the vortex reaches the boundary of the condensate at $y_0 = 4.2$ for $g = 100$ and at $y_0 = 7.2$ for $g = 500$.

even higher values the range of velocity for which the pair of rarefaction waves exist will diminish and eventually tend to zero. Furthermore, the number of vortices in the channel can be estimated for each branch. Two vortices are expected to be present in the lowest branch and a further two added to the channel at each cusp all the way to the highest branch, whereupon a black soliton can be expected to appear for zero velocity and maximal energy ($p = \pi$).

Brand and Reinhardt [34] have given compelling numerical evidence that the branch of solitonic vortices joins the branch of dark solitons in a box potential when the width of the condensate is reduced to a few healing lengths. This may suggest that there exists another critical coupling g for which the two branches depicted in Figs. 7 and 8 completely overlap. Similarly, it may suggest that for p close to 0 and π the corresponding branches join via a bifurcation for all g.

VI. CONCLUSION

In summary, we considered the effects of the boundaries and inhomogeneities of the density backgrounds on the vortex motion using numerical solutions and asymptotics. We showed that the method of images together with the Hamiltonian group relation is a useful tool for finding the velocity of a quantum vortex. We showed that the image vortex plays an important role not only when the vortex moves close to the condensate surface, where the distance to the image is small, but gives the dominant contribution to the velocity of a vortex that moves close to the center of the condensate where the density gradients are small because of an effective 'shift' in the position of the image caused by the large density depletion at the boundary.

Travelling coherent structures moving in an infinitely long two-dimensional channel in the presence of a harmonic trap were analyzed in some detail and the approximation of the vortex velocity was found.

ACKNOWLEDGMENTS

NGB is grateful to EPSRC-UK support and to Dr. Joachim Brand for many useful discussions. PM would like to thank Dr. Stavros Komineas for useful discussions.

[1] L. M. Pismen, *Vortices in Nonlinear Fields* (Clarendon Press, Oxford, 1999).
[2] M. R. Matthews et al., Phys. Rev. Lett. **83**, 2498 (1999).
[3] C. Raman et al., Phys. Rev. Lett. **87**, 210402 (2001).
[4] M. R. Andrews et al., Phys. Rev. Lett. **79**, 553 (1997).
[5] Z.Dutton et al., Science **293**, 663 (2001).
[6] B. P. Anderson et al., Phys. Rev. Lett. **86**, 2926 (2001).
[7] S. Burger et. al., Phys. Rev. Lett. **83**, 5198 (1999).
[8] J. Denschlag et al., Science **287**, 97 (2000).
[9] A. L. Fetter and A. A. Svidzinsky, J. Phys.: Condens. Matter **13**, R135 (2001).
[10] L. D. Carr and J. Brand, cond-mat/0705.1139.
[11] L. P. Pitaevskii and S. Stringari, *Bose-Einstein Condensation* (Clarendon Press, Oxford, 2003).
[12] B. Y. Rubinstein and L. M. Pismen, Physica D **78**, 1 (1994).
[13] Y.S.Kivshar, J. Christou, V. Tikhonenko, B. luther-Davies, and L.M. Pismen, Optics Comm. **152**, 198 (1998).
[14] J. R. Anglin, Phys. Rev. A **65**, 063611 (2002).

[15] J.-P. Martikainen et al Phys. Rev. A **64**,063602 (2001); P.O. Fedichev and G.V. Shlyapnikov, Phys. Rev. A **60**, R1779 (1999); Schulte et al Phys. Rev. A **66**, 033602 (2002).
[16] P. Mason, N. G. Berloff and A. L. Fetter, Phys. Rev. A **74**, 043611 (2006).
[17] E. Lundh and P. Ao, Phys. Rev. A **61**, 063612 (2000).
[18] H. M. Nilsen, G. Baym, and C.J.Pethick, Proc. Natl. Acad. Sci. **103**, 7978 (2006).
[19] E. Lundh, C.J. Pethick, and H. Smith, Phys. Rev. A **55**, 2126 (1997).
[20] D. S. Naik, S. R. Muniz and C. Raman, Phys. Rev. A **72**, 051606(R) (2005).
[21] N. Ginsberg et al Phys. Rev. Lett. **94**, 040403 (2005).
[22] S. Komineas and N. Papanicolaou, Phys. Rev. Lett. **89**, 070402 (2002).
[23] S. Komineas and N. Papanicolaou, Phys. Rev. A **67**, 023615 (2003).
[24] S. Komineas and N. Papanicolaou, Phys. Rev. A **68**, 043617 (2003).
[25] L. Carr et al, J. Phys. B: At. Mol. Opt. Phys. **33**, 3983 (2000)
[26] J. Brand and W. P. Reinhardt, J. Phys. B: At. Mol. Opt. Phys., **34**, L113 (2001)
[27] S. Komineas and J. Brand, Phys. Rev. Lett., **95**, 110401 (2002).
[28] W. Bao et al J. Comp. Phys. **187**, 318 (2003).
[29] C. A. Jones and P. H. Roberts, J. Phys. A: Gen. Phys. **15**, 2599 (1982).
[30] U. Al Khawaja, Phys. Rev. A **71**, 063611 (2005).
[31] J. Kim and A. L. Fetter, Phys. Phys. Rev. A **70**, 043624 (2004).
[32] L. D. Carr and C. W. Clark, Phys. Rev. A **74**, 043613 (2006).
[33] D. L. Feder et al., Phys. Rev. A **62**, 053606 (2000).
[34] J. Brand and W. P. Reinhardt, Phys. Rev. A, **65**, 043612 (2002).
[35] T. Tsuzuki *J. Low Temp. Phys.* **4** 441 (1971).
[36] N.G. Berloff, *J. Phys. A: Math. Gen.* **37**, 1617 (2004).
[37] A. E. Muryshev, N. B. van Linden van den Heuvell and G. V. Shlyapnikov, Phys. Rev. A **60**, R2665 (1999).
[38] P. K. Newton, *The N-Vortex Problem* (Springer, 2001).